

The inclusion of secondary protons via convolutional methods

V. Gajadhar



The inclusion of secondary protons via convolutional methods

by

V. Gajadhar

to obtain the degree of Bachelor of Science
at the Delft University of Technology,
to be defended publicly in August 2022

Student number: 5056535
Project duration: April 18, 2022 – July 18, 2022
Thesis committee: dr. Z. Perko, TU Delft, supervisor
dr. ir. D. Lathouwers TU Delft
T. Burlacu TU Delft

This thesis is confidential and cannot be made public until July 31, 2022.

An electronic version of this thesis is available at <http://repository.tudelft.nl/>.

Preface

I would like to thank T. Burlacu for his support, flexibility and guidance during the research and writing of my thesis. Also, I would like to thank Z. Perko for his advice, flexibility and critical eye during the research and writing of my thesis.

V. Gajadhar
Delft, July 2022

Abstract

Dose calculations in proton therapy need to be computed as fast as possible for successful cancer treatment planning and execution. The dose calculation algorithms that provide enough accuracy for treatment planning, takes too much time to utilise; therefore there is a need for faster alternatives. One of the alternatives is using a deterministic semi-analytic numerical algorithm for EM interactions. This alternative in its current state is not accurate enough, and therefore it is sought to include the effects of secondary protons on the total dose distribution of the deterministic semi-analytic numerical algorithm, using convolutional methods. In this thesis an attempt is made to find a kernel that, when convoluted with a primary proton flux, produces the desired secondary proton dose. The parameters of two different types of kernels, the Gaussian kernel and Fractional Filter kernel, are optimised and their resulting shapes are presented. Furthermore, the secondary proton dose through the convolution of the primary proton flux and the different kernels are presented. The doses obtained from the optimal kernels are compared with the target dose on the shape and a measure of quality: the gamma index passing rate. Found was that the Fractional Filter kernel can produce both asymmetric doses and symmetric doses, while the Gaussian kernel can only produce symmetric doses. The passing rate was found to be 29.41% for the Fractional Filter kernel and 17.65% for the Gaussian kernel. Thus, the Fractional Filter is better for estimating secondary proton dose distribution through convolutional methods than using a Gaussian kernel. but insufficient due to the low passing rate. A suggestion for improvement is applying skew-Gaussians in the Fractional Filter kernel or by applying other asymmetric kernels.

Contents

1	Introduction	1
1.1	Cancer	1
1.2	Radiotherapy	1
1.2.1	Radiotherapy in general	1
1.2.2	Proton therapy	1
1.2.3	Treatment planning	2
1.3	Outline Thesis	2
2	Material and methods	3
2.1	Proton interactions in matter	3
2.1.1	Inelastic Coulomb interaction	3
2.1.2	Elastic Coulomb scattering	3
2.1.3	Non-elastic nuclear interaction	3
2.2	Proton transport	4
2.3	Dose calculation	4
2.3.1	Monte Carlo	4
2.3.2	Pencil beam dose calculation through convolution	4
2.4	Inclusion of secondary protons contribution through kernel optimisation	6
2.4.1	Optimisation problem	6
2.4.2	Kernel shapes	6
2.5	Comparing two doses	8
2.5.1	Integrated depth dose	8
2.5.2	Gamma index	8
3	Results and discussion	9
3.1	TOPAS dose and flux	9
3.2	Kernel Shape	12
3.2.1	Kernel parameters	12
3.3	Dose comparison	15
3.3.1	Doses through convolution	15
3.3.2	Gamma index comparison	19
3.3.3	Comparison of the convolutional dose distributions	20
4	Conclusion and recommendations	21
4.1	Conclusion	21
4.2	Recommendations for further research	21

Introduction

1.1. Cancer

In 2018, 18.1 million people around the world had cancer and 9.6 million people died from the disease. It is expected that these numbers will double by 2040; therefore there is a high demand for improving and developing methods to effectively treat cancer [1]. Cancer is a disease in which groups of abnormal cells grow and invade the surrounding tissue. Because there are trillions of cells in the human body, cancer can originate almost anywhere. Normal cells in a human body divide and reproduce themselves to form new cells as the body needs them. Old and damaged cells die and new cells take their place. This process sometimes malfunctions: abnormal or damaged cells grow and multiply when they should not, causing the forming of tumors. Tumors can be cancerous or not cancerous. Cancerous tumors are able to spread into nearby tissues and can travel to distant places in the body to form new tumors. [2]. Some conventional ways to fight tumors before they can do serious damage to the body are: surgery, radiation therapy, and chemotherapy. Some more unconventional ways are the use of drugs, biological molecules, and immune-mediated therapies [3]. This study is focused on a specific branch of radiotherapy, namely proton therapy.

1.2. Radiotherapy

1.2.1. Radiotherapy in general

The radiation used in radiotherapy is called ionizing radiation because it causes the forming of ions and deposits energy in cells of the tissue that it passes through. Cancer cells can be killed by the energy that is deposited, either directly or by causing genetic changes that result in the death of a cancer cell. A problem with high-energy radiation is that it damages genetic material (DNA) of both cancer cells and normal healthy cells [4]. Therefore, the goal of radiation therapy is to maximize the radiation dose to the cancer cells while minimizing radiation exposure to normal cells, that are next to cancer cells or in the radiation path. There are two different ways of delivering radiation to a cancer cell: external and internal radiation. External radiation uses high-energy rays (photons, protons or particles) for radiating the cancer cells, by aiming the rays to the location of the tumor. Internal radiation makes use of radioactive sources inside the body to radiate the tumors. These radioactive sources are sealed into catheters or seeds, which are implanted into the tumor site [5].

1.2.2. Proton therapy

Proton therapy is a promising method of utilising radiotherapy, when compared with the conventional method of photon therapy. This is because highly localized dose distributions are achieved by proton beams that would result in higher probabilities for local control and disease-free survival, and lower probabilities for normal tissue damage [6]. This can be seen in figure 1.1, where the dose distribution of a 15 MV photon beam and a proton beam are compared to an ideal dose distribution.

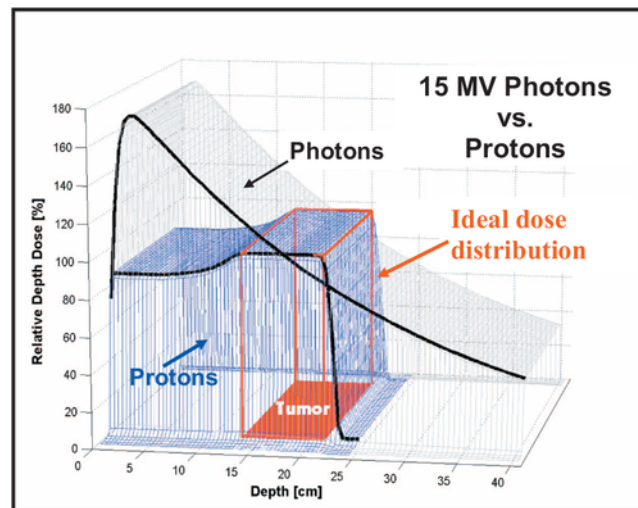


Figure 1.1: Comparison of depth dose curves for 15 MV photons and a spread Bragg peak. Shown in red is an ideal dose distribution, which provides a uniform, maximum dose to the target volume and zero dose outside the target volume. The proton dose distribution approaches the ideal case to a much greater extent compared to the photon dose distribution. Furthermore, an important factor is the steep falloff after the dose maximum for the proton distribution. Source: [6].

1.2.3. Treatment planning

Treatment planning for radiotherapy is a procedure that produces machine instructions for the used machines (e.g. beam energy) and the expected dose distribution in the patient [7]. To make such a treatment planning a model of the radiation beam and of the patient's anatomy (CT-scan) needs to be considered. Treatment planning procedures for different radiation types do have some common characteristics, however using protons as a radiation type comes with some implications. The properties that make protons interesting for radiotherapy are also the cause for these implications; namely the precision of the energy deposition (Bragg Peak) needs to be even greater compared to the usage of other radiation types [7].

At the moment the most accurate method is the Monte Carlo method, which is often referred to as the 'golden standard'. This algorithm determines the dose distribution very accurately. A downside of this method is the long time of computation that deems it clinically unfeasible. Therefore, research is being done to find a more practical yet accurate substitute for the Monte Carlo algorithm for treatment planning in proton therapy. [8].

1.3. Outline Thesis

In this thesis, research is done on improving the accuracy of an already existing semi-analytic dose calculation algorithm, which proves to be very time-efficient, such that it is practical (time-wise) for treatment planning. To obtain this improvement on the accuracy, the focus will be on finding an optimal kernel that provides accurate secondary proton doses, via convolutional methods.

In chapter 2, an introduction about proton interactions in a medium will be given, followed by an explanation of the convolution algorithm and the method for including the contribution due to secondary protons. Subsequently, in chapter 3, the results from implementing the method for including the secondary protons will be presented and discussed. Lastly, in chapter 4 a conclusion will be drawn from the results and discussion, which is followed by recommendations for future research.

This report is part of a bachelor thesis research of Technology University of Delft at the department of Medical Physics Technology at the Reactor Institute Delft.

2

Material and methods

2.1. Proton interactions in matter

When protons are propagating through the body there are different kinds of interactions that can occur, with the surrounding matter. Mainly, there are three different kind of interactions that need to be considered: inelastic Coulomb interaction, elastic Coulomb scattering and non-elastic nuclear interaction [9]. Another interaction that is theoretically possible is proton Bremsstrahlung, but at therapeutic proton beam energies this effect is negligible [10].

2.1.1. Inelastic Coulomb interaction

When protons propagate through matter, their interactions with atomic electrons can be described by inelastic Coulomb scattering. Through this interaction, the proton loses some of its energy due to the fact that the electron and the proton attract each other. The attraction occurs due to the fact that electrons are negatively charged and the protons are positively charged. However, because of the relative small mass of the electron compared to the proton, the proton's trajectory only changes very little. So the proton loses kinetic energy continuously, but diverges only slightly from its original trajectory because of the inelastic Coulomb interaction. Thus, in this interaction kinetic energy is not conserved, but the particle type remains unchanged. [10].

2.1.2. Elastic Coulomb scattering

A proton passing close to an atomic nucleus experiences a repulsive force due to the Coulomb force. This force is caused by the positive charge of both the proton and atomic nuclei. In contrast with the inelastic Coulomb interaction, this interaction changes the former straight-line trajectory of the proton, but does only have a small influence on its energy. In this interaction, the kinetic energy and particle type both remain unchanged [10].

2.1.3. Non-elastic nuclear interaction

The non-elastic nuclear interaction has a more profound effect on the proton compared to the Coulomb interactions. The proton enters a nucleus and is absorbed. This absorption causes the forming of what is called secondary particles. During such a reaction different kinds of secondary particles can be created: protons, deuterons, tritons, neutrons, or heavier ions (Helium). These secondary particles can have a significant contribution to the particle dose [11]. So due this interaction both kinetic energy and particle type changes. For this research the focus will be on including secondary protons into the dose calculation.

2.2. Proton transport

In order to describe proton transport, the Linear Boltzmann Equation (LBE) is used as derived by Duderstadt and Hamilton [12]. The LBE is mathematically described as in Equation 2.1:

$$\hat{\Omega} \cdot \nabla \Phi(\vec{r}, E, \hat{\Omega}) + \sigma_t \Phi(\vec{r}, E, \hat{\Omega}) = \int_{4\pi} \int_0^\infty dE' \sigma_s(\vec{r}, E' \rightarrow E, \hat{\Omega}' \rightarrow \hat{\Omega}) \Phi(\vec{r}, E', \hat{\Omega}') d\hat{\Omega}', \quad (2.1)$$

where 2.1 \vec{r} is the position of the particle, Φ is the proton flux, $\hat{\Omega}$ is the direction of the particle, E is the energy of the particle, σ_t is the total cross section and σ_s is the total scatter cross section. The first term on the left-hand side of Equation 2.1 is representing the flow of non-interacting particles. The second term on the left-hand side describes the particles that interact so that their initial direction $\hat{\Omega}$ and energy E are modified. The right-hand side of Equation 2.1 describes particles that start with direction $\hat{\Omega}'$ and energy E' that end up with direction $\hat{\Omega}$ and energy E , due to an interaction [13]. With the use of several approximations, the LBE is transformed into the Fokker-Planck equation and the Fermi-Eyges equation[14], which are two partial differential equations. From these equations the proton flux Φ is obtained, which is a quantity that contains information on how the protons move through a certain medium. The proton flux is used to determine the proton dose distribution.

2.3. Dose calculation

A good dose calculation is very important for proper proton treatment of the patients. There are many variables involved in a proton treatment plan, such as the amount of protons, the target location of the protons and the gantry angle of the protons. To obtain the best choice for the different variables, the patient must be scanned. The scan contains information about the location of the tumor and all surrounding organs. An objective function that aims to maintain a high dose in the tumor and a low dose in the surrounding tissue is therefore minimised. Many dose calculations must be performed to optimise the treatment plan.

2.3.1. Monte Carlo

The Monte Carlo method tracks the trajectory of every single proton in a simulated proton beam. The method tracks the trajectories of protons in small steps. For each of these steps, the algorithm randomly samples from probability distributions. These distributions contain information about the chance for different kinds of interactions to happen based on the energy and trajectory of the proton at that specific moment [15]. The number of protons in a typical therapeutic proton beam is in the order of 10^9 [16]. Because of the high number of protons and the individual tracking of these protons, the computation of a simulation with this method takes a lot of time. A useful Monte Carlo algorithm for medical purposes is the TOPAS algorithm [17]. TOPAS is an extension of the Geant4 Simulation Toolkit, which makes advanced Monte Carlo simulation easier accessible for medical physicists. In this research, the dose obtained through convolutional methods will be compared to the TOPAS dose.

2.3.2. Pencil beam dose calculation through convolution

A way of cheaply computing a dose distribution is by using a convolutional method. This calculation is mathematically formulated in Equation 2.2:

$$D_c(x, y, z) = \Phi * K = \sum_k \sum_l \sum_m \Phi(x, y, z) K(x - k, y - l, z - m), \quad (2.2)$$

where D_c is the dose through convolution, Φ is the proton flux and K is the convolution kernel [18]. Filters for this method can be applied from the field of imaging filter processing due to the similarity of the mathematical operations involved [19]. The difference is that for proton therapy, the kernel, flux and dose are 3-dimensional matrices instead of 2-dimensional.

Convolution

A convolution is a mathematical operation that is described in Equation 2.3 for (3D) discrete functions [20]. Since the application of convolution is only needed for matrices the definition for continuous functions is not discussed, however both discrete and continuous convolution work in the same way.

$$(f * g)[i, j, k] = \sum_{n=-\infty}^{\infty} \sum_{m=-\infty}^{\infty} \sum_{l=-\infty}^{\infty} f[i, j, k]g[i - n, j - m, k - l] \quad (2.3)$$

Convolution intuitively measures the overlap between two functions. To understand convolution of matrices intuitively, a 2-D example is used, as shown in Figure 2.1. The kernel in Figure 2.1 is a two-dimensional 3x3 matrix of weights, which is dragged across the image. The filter is applied to an area of the image, and a dot product is calculated between the input pixels of the image and the filter. This dot product is contained into an output array. The filter moves across the whole image repeating the process until the filter has moved across the whole image. The output matrix is typically the same size as the input matrix. The same procedure can be applied for 3-D matrices.

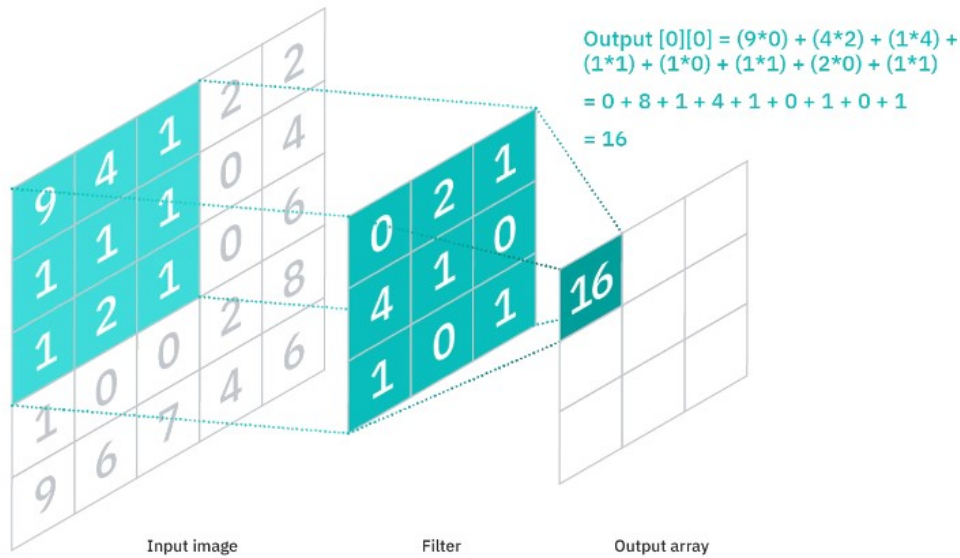


Figure 2.1: Illustration of the convolutional process of two 2D matrices. Source: [21]

2.4. Inclusion of secondary protons contribution through kernel optimisation

2.4.1. Optimisation problem

To find an optimal kernel an optimisation process is carried out. To this end, the objective function is defined as in Equation 2.4 :

$$SSE = \sum_{i,j,k} (D_{MC}(i,j,k) - D_c(i,j,k))^2 = \sum_{i,j,k} (D_{MC}(i,j,k) - (\Phi * K(\vec{\theta})))(i,j,k))^2, \quad (2.4)$$

where D_{MC} is the secondary proton dose from the Monte Carlo algorithm, Φ is the primary proton flux and K is the kernel with parameters $\vec{\theta} = [\theta_1, \theta_2, \dots, \theta_n]$ that needs to be optimised [22]. The kernel can be obtained by minimising the SSE, which turns finding the optimal kernel into an optimisation problem.

Optimising in Python

The optimisation was performed using the Python `scipy.optimize` library. From this library the algorithm `scipy.optimize.fmin` was used, which uses the simplex downhill algorithm [23]. Also, the algorithm `scipy.optimize.fmin_cg` was used, which uses the conjugate gradient method [24]. Depending on the type and shape of the kernel, a choice can be made on what optimisation algorithm to use.

2.4.2. Kernel shapes

This section describes the general shapes of the kernels that were optimised.

Gaussian kernel

The Gaussian kernel is one of the most commonly used kernels in imaging and is often used in medical physics as a kernel [25]. The Gaussian kernel is used for smoothing an image and can be described in 3D as in Equation 2.5:

$$g(x, y, z) = \exp\left(-\frac{(x - x_c)^2 + (y - y_c)^2}{2\sigma_{xy}^2} - \frac{(z - z_c)^2}{2\sigma_z^2}\right), \quad (2.5)$$

where x_c, y_c, z_c determine the position of the center of the Gaussian kernel and σ_{xy} and σ_z determine the spread of the Gaussian kernel in x-y and z direction respectively [26]. The 3D Gaussian kernel can have different kinds of matrix sizes, commonly used matrix sizes are 3x3x3, 5x5x5 or 7x7x7. For an illustration of the Gaussian kernel shape, a 2D 3x3 sized Gaussian kernel is shown in Figure 2.2.

0.075	0.124	0.075
0.124	0.204	0.124
0.075	0.124	0.075

Figure 2.2: An example of a 3x3 Gaussian kernel where the parameters x_c and y_c are zero.

Sobel kernel

The Sobel kernel is used for edge detection in image processing [27]. The doses are expected to have regions with large gradient differences, the Sobel kernel is meant for mapping these types of regions. For every direction there is a different Sobel operator, for example for a 2D image there are 2 Sobel operators one for gradient detection in the x-direction and one for the y- direction. 3x3 Sobel operators in x and y-direction are given by:

$$S_x = \begin{bmatrix} -1 & 0 & 1 \\ -2 & 0 & 2 \\ -1 & 0 & 1 \end{bmatrix}, \quad S_y = \begin{bmatrix} -1 & -2 & -1 \\ 0 & 0 & 0 \\ 1 & 2 & 1 \end{bmatrix}. \quad (2.6)$$

A 3D extension of the Sobel operator can be done in x,y and z directions. For example, the 3x3x3 Sobel operator in z-direction is given as:

$$S_z(:, :, -1) = \begin{bmatrix} -1 & -2 & -1 \\ -2 & -4 & -2 \\ -1 & -2 & -1 \end{bmatrix}, \quad S_z(:, :, 0) = \begin{bmatrix} 0 & 0 & 0 \\ 0 & 0 & 0 \\ 0 & 0 & 0 \end{bmatrix}, \quad S_z(:, :, 1) = \begin{bmatrix} 1 & 2 & 1 \\ 2 & 4 & 2 \\ 1 & 2 & 1 \end{bmatrix}, \quad (2.7)$$

where the presented 2D matrices are slices of the 3D matrix [28].

Fractional Filter kernel

The Fractional Filter (FF) is a combination of the Gaussian kernel, Sobel Kernel, Laplacian Kernel [29] and Mexican-Hat filters [29]. The Sobel filter approximates the first derivative of the Gaussian filter [30]. The Laplacian filter is defined as the second derivative of the Gaussian Filter and the Mexican hat filter is the sign-inverted second order derivative of the Gaussian filter [31]. So these different types of kernels are related through the derivatives of the Gaussian filter. It is possible to summarise all of these filters into one filter by using the theory of fractional calculus [32]. This filter is shown in Equation 2.8 :

$$F(x, y, z) = AD^a e^{-\frac{(x-x_c)^2}{2\sigma_x^2}} D^b e^{-\frac{(y-y_c)^2}{2\sigma_y^2}} D^c e^{-\frac{(z-z_c)^2}{2\sigma_z^2}}, \quad (2.8)$$

where $A \in (-\infty, \infty)$ is some amplitude term, $a, b, c \in (0, 2)$ is the order of the fractional derivative in x, y and z direction respectively and $x_c, y_c, z_c \in (-\infty, \infty)$ and $\sigma_x, \sigma_y, \sigma_z \in (0, \infty)$ are the parameters of a Gaussian kernel [33]. The fractional derivative of a Gaussian function can be approximated using a Taylor series (up to 15th order for computational efficiency) as described in Equation 2.9:

$$D^a G(x) = \frac{A_x}{h^a} \sum_{n=0}^{15} \frac{\Gamma(a+1)G(x)}{(-1)^n \Gamma(n+1)\Gamma(1-n+a)}, \quad (2.9)$$

where $\Gamma(n) = (n-1)!$ [33]. Notice that constant A_x in Equation 2.9 is a different constant than A in Equation 2.8. The constant A is the product of the constants of the fractional derivative in the x, y and z direction.

2.5. Comparing two doses

2.5.1. Integrated depth dose

Next to presenting slices of the 3D doses, a one-dimensional representation will be used to present the doses, such that differences between the doses are easier to visualize. This one-dimensional representation is the integral depth dose (IDD) and is shown in Equation 2.10:

$$IDD(z) = \sum_{x=0}^m \sum_{y=0}^n D(x, y, z) \Delta x \Delta y, \quad (2.10)$$

where Δx and Δy are the bin size in x and y direction respectively [34].

2.5.2. Gamma index

A commonly used verification of the difference between the two doses is the gamma index. The gamma index combines dose difference and distance difference to calculate a dimensionless metric for each point between the reference dose and the dose that needs to be evaluated [35]. The gamma value is determined via Equation 2.11:

$$\gamma = \min \left(\sqrt{\frac{(\vec{r}_e - \vec{r}_c)^2}{\Delta r^2} + \frac{(D_e(\vec{r}_e) - D_c(\vec{r}_c))^2}{\Delta D^2}} \right), \quad (2.11)$$

where \vec{r}_e is a point in the exact dose distribution, \vec{r}_c a point in the comparing dose distribution, ΔD is the dose difference criterion, Δr is the distance-to-agreement criterion and D_e and D_c are the exact and comparison dose respectively [36]. If the value of the gamma at a specific point voxel is smaller than 1, then this point is accepted. So a passing rate can be introduced, which is the amount of gamma voxels that have a value smaller than 1 divided by the total amount of voxels [37]. As a measure to see how much the pencil beam dose improves from adding secondary protons, the dose from the deterministic semi-analytic algorithm with and without the convolved secondary proton dose can be compared to the Monte Carlo dose through gamma index.

3

Results and discussion

3.1. TOPAS dose and flux

The geometry used is a simple water box of 5 cm x 5 cm x 10 cm in the x, y and z (depth) direction respectively. The water box is divided into voxels of 0.098 cm x 0.098 cm x 0.1 cm (or 51 x 51 x 100 bins).

Primary proton flux

The primary proton flux can be seen as a beam of protons that is moving through the water box. In Figure 3.1 the proton flux is shown in the x-y plane sliced at $z = 5$ cm. In figure 3.2 the proton flux is shown in the y-z plane sliced at $x_{bin} = 25$, which is in the middle. The x-z plane is similar to the y-z plane and is therefore not plotted.

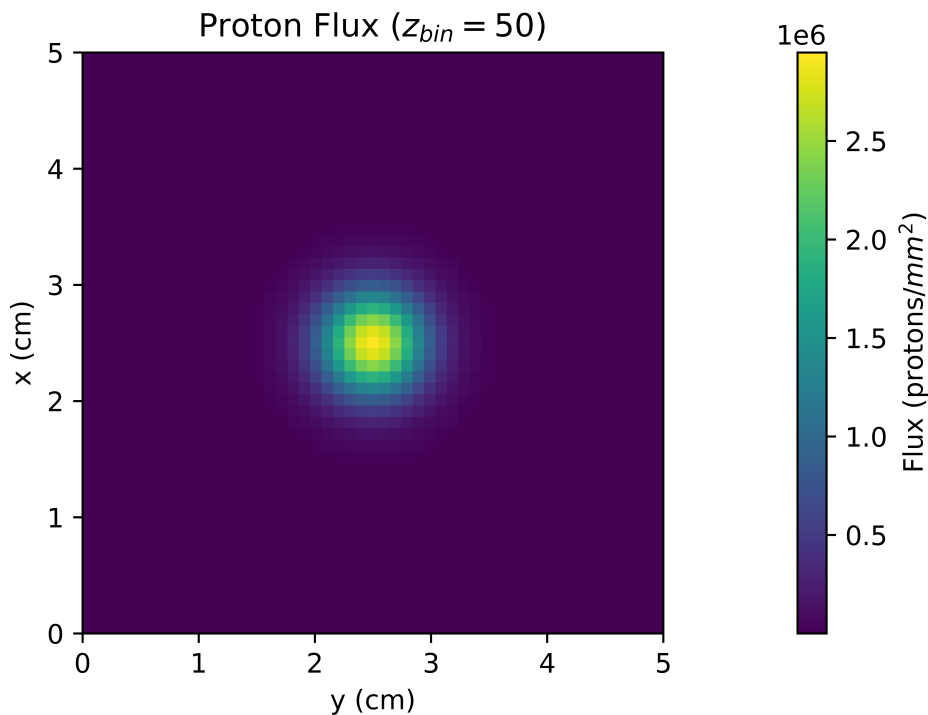


Figure 3.1: The primary proton flux shown from the x-y plane. The slicing was done in the middle at $z_{bin} = 50$ or $z = 5$ cm. The proton flux is symmetric in the x-y plane.

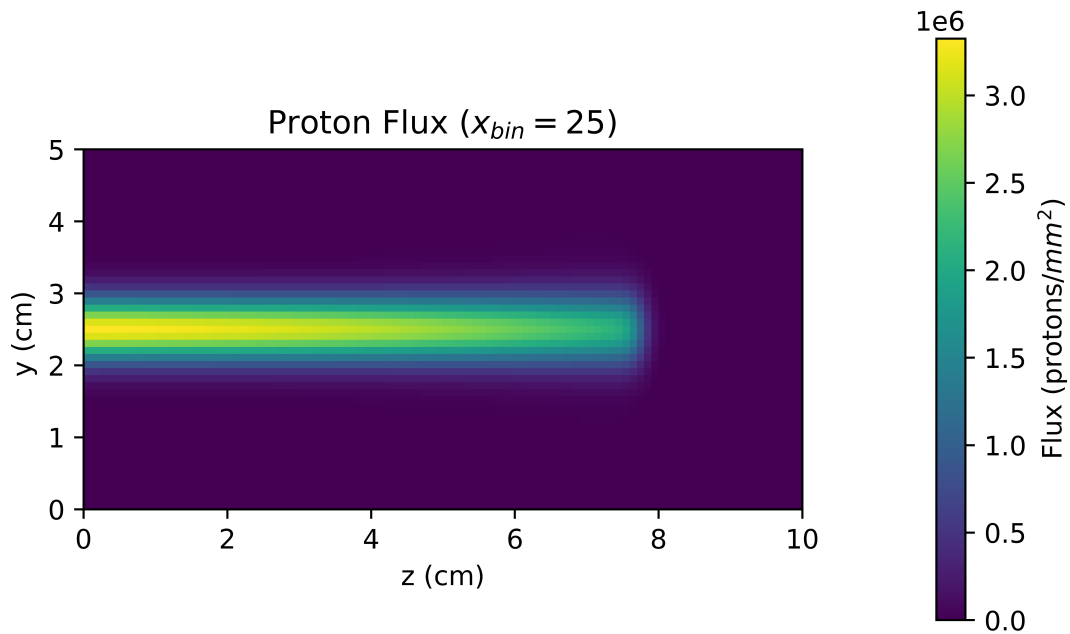


Figure 3.2: The primary proton flux shown from the y-z plane. The slicing was done around the middle at $x_{bin} = 25$. Note that the x-z plane looks similar to the y-z plane due to symmetry.

TOPAS dose

The secondary proton dose is scored with phase space scorers through the use of test boxes (1,5 cm x 1,5 cm x 0.04 cm) that are set up throughout the box from 0.5 cm up to 9.5 cm in steps of 1 cm. From these test surfaces the creation of secondary protons is simulated. The secondary proton distributions are then stored into a separate file for each test box [38]. In Figure 3.3 the setup of the test boxes is shown.

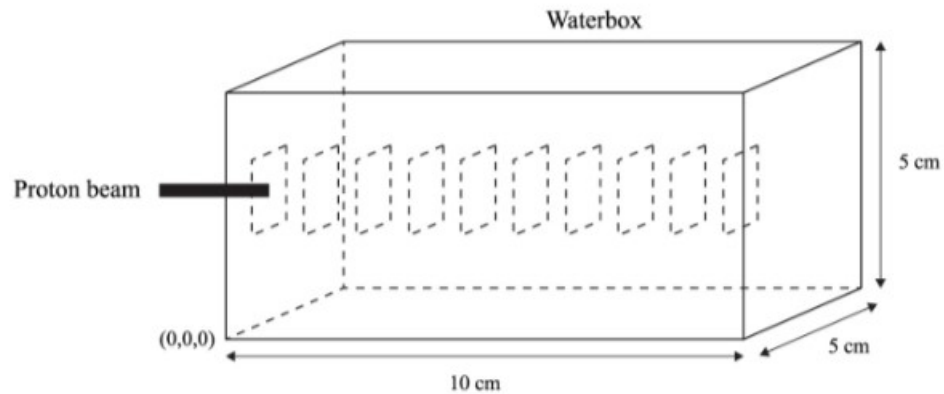


Figure 3.3: The setup that is used to score secondary protons with the use of phase space scorers. The dotted boxes are the test boxes which are assigned a phase space scorer. Note that the lateral shape of these testboxes is so small to show. Source: [38]

In Figure 3.4, the secondary proton dose from the first test box at 0.5 cm is shown in the x-y plane, similar to Figure 3.1. In Figure 3.5 the same dose is shown in the y-z plane, similar to Figure 3.2, but only zoomed into a specific region.

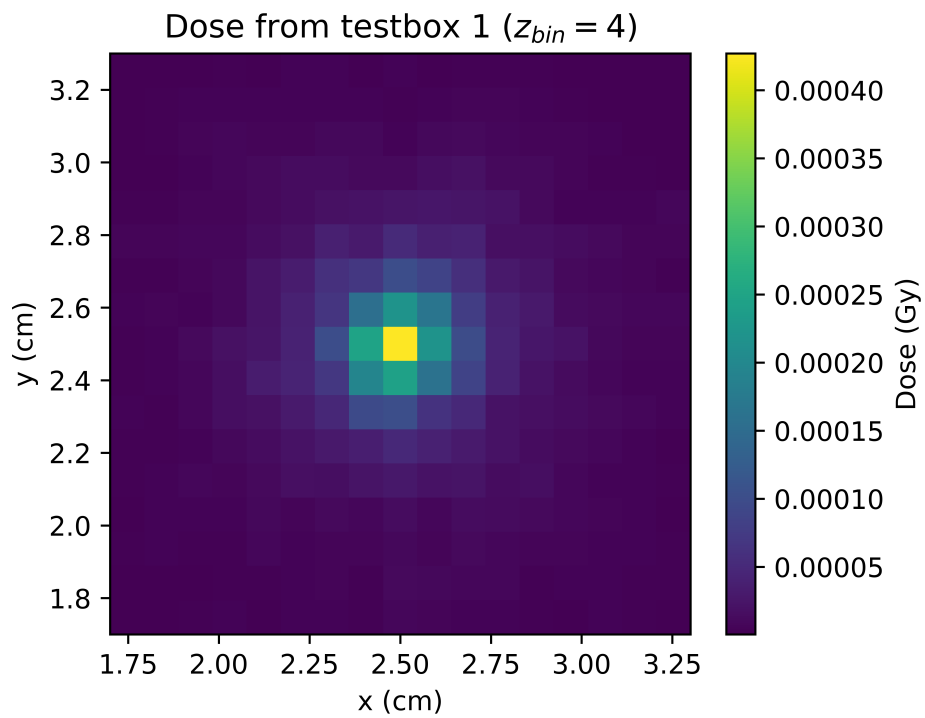


Figure 3.4: The secondary proton dose due test surface 1 located at 0.5 cm in z-direction, shown from the x-y plane. The slicing was done in the middle at $z_{bin} = 4$ or $z = 0.4$ cm. Note that the plot is zoomed into the region from 1.7-3.3 cm in both x and y directions. This is to have a better view of the shape of the dose.

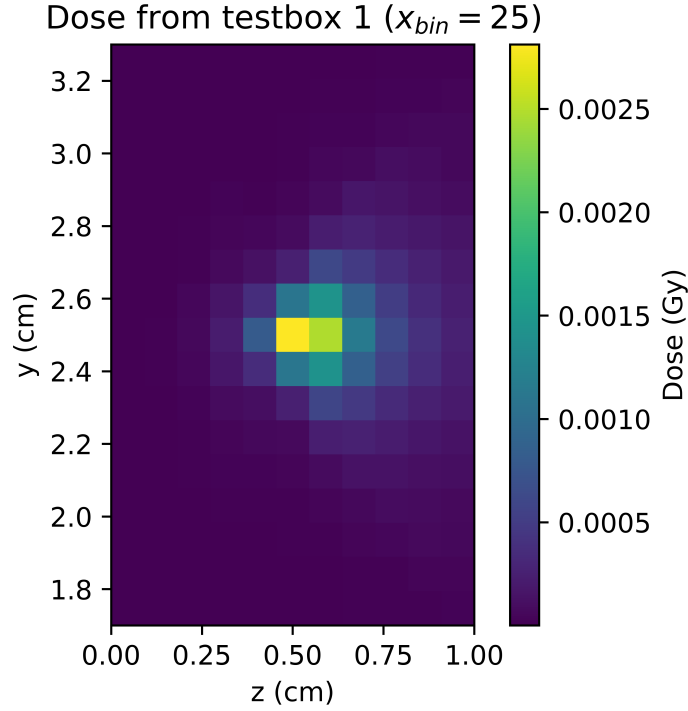


Figure 3.5: The secondary proton dose due test surface 1 located at 0.5 cm in z-direction, shown from the x-z plane. The slicing was done in the middle at $x_{bin} = 25$. Note that the plot is zoomed into the region from 0-1.0 cm in the z-direction and into the region from 1.7-3.3 cm in the y direction. This is to have a better view of the shape of the dose. The dose is non-symmetric and forward scattered in the +z direction.

3.2. Kernel Shape

3.2.1. Kernel parameters

Two different types of kernels were used: the Gaussian kernel and the Fractional Filter (Section 2.4.2). These kernels were fitted with the primary proton dose and secondary proton flux described in Section 3.1. The doses obtained from both kernels and the dose from Section 3.1 will be compared later on in Section 3.3

Gaussian Kernel shape and parameters

The dose presented in Figure 3.4 is slightly asymmetrical in the x and y direction, therefore the Gaussian kernel from Section 2.4.2 has been altered by splitting σ_{xy} into σ_x and σ_y . Also an amplitude A term has been added, resulting in the following kernel:

$$g(x, y, z) = A \exp\left(-\frac{(x - x_c)^2}{2\sigma_x^2} - \frac{(y - y_c)^2}{2\sigma_y^2} - \frac{(z - z_c)^2}{2\sigma_z^2}\right). \quad (3.1)$$

In this kernel, optimal parameters were found through the optimisation process described in Section 2.4.1. The optimal parameters for the Gaussian kernel are presented in table 3.1 and the shape is shown in Figure 3.6. The optimisation of the parameters took 17.5 seconds with an SSE value of $1 \cdot 10^{-4} \text{ Gy}^2$.

$$\begin{aligned} A &= 1.52 \cdot 10^{-9} \text{ Gy} \cdot \text{mm}^2 & x_c &= 1.09 \text{ cm} \\ \sigma_x &= 2.72 \text{ cm} & y_c &= 1.18 \text{ cm} \\ \sigma_y &= 9.43 \cdot 10^{-1} \text{ cm} & z_c &= 1.02 \text{ cm} \\ \sigma_z &= 1.32 \text{ cm} \end{aligned}$$

Table 3.1: Optimal parameters found for the Gaussian kernel from Equation 3.1.

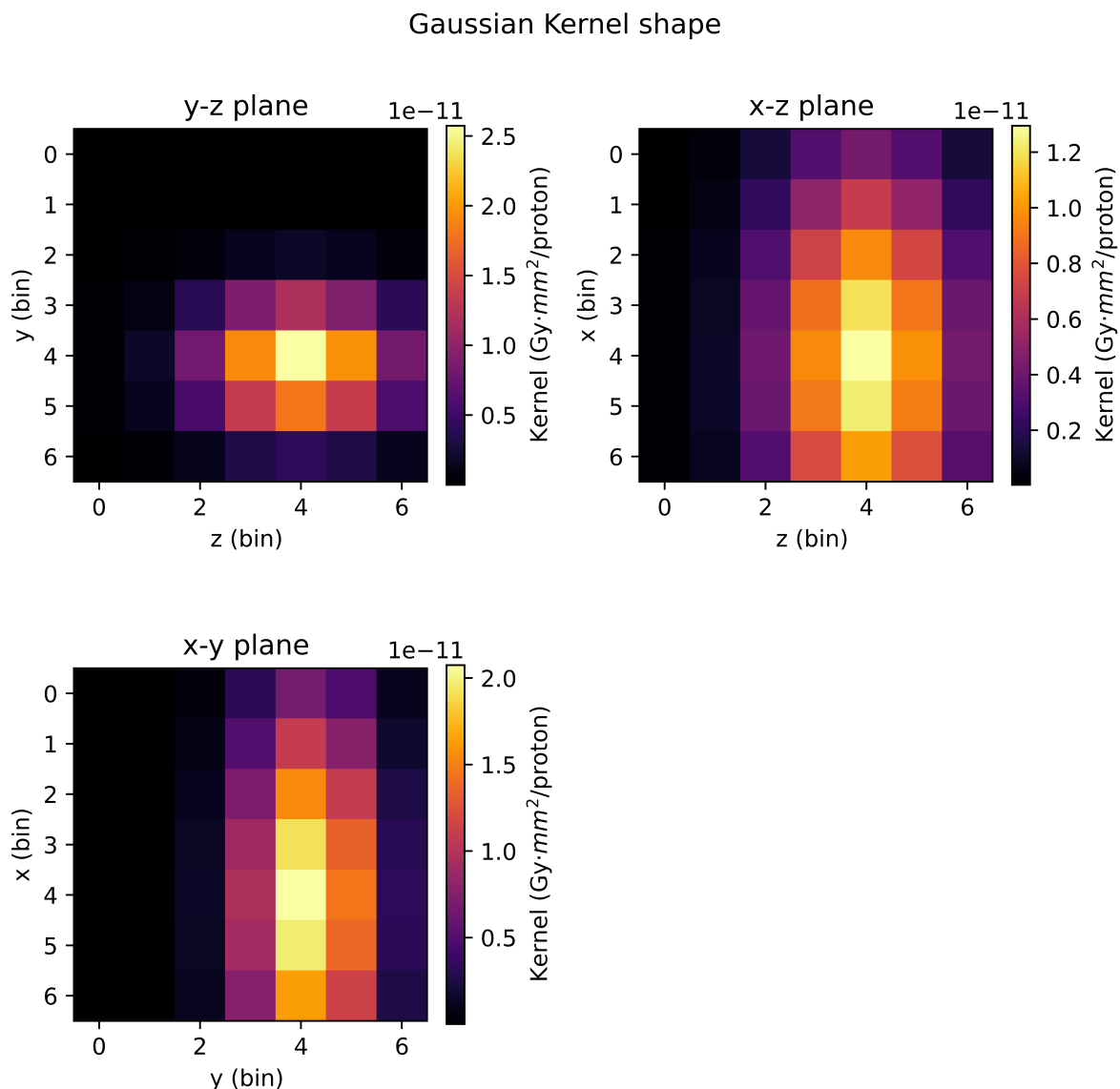


Figure 3.6: 7x7x7 Gaussian kernel; in the y-z plane sliced at $x_{bin} = 4$, in the x-z plane sliced at $y_{bin} = 4$ and in the x-y plane sliced at $z_{bin} = 4$.

Fractional Filter kernel shape and parameters

The parameters of the FF kernel were found according to Section 2.4.1. The optimal parameters for the FF Kernel are presented in table 3.2 and the shape is shown in Figure 3.7. The optimisation of the parameters took 68.9 seconds with an SSE value of $1 \cdot 10^{-4}$ Gy².

$$\begin{array}{lll}
 A = 36.2 \text{ Gy} \cdot \text{mm}^2 & x_c = -0.12 \text{ cm} & a = 1.31 \\
 \sigma_x = 3.93 \text{ cm} & y_c = -0.05 \text{ cm} & b = 1.33 \\
 \sigma_y = 0.29 \text{ cm} & z_c = 2.75 \text{ cm} & c = 2.20 \\
 \sigma_z = 1.63 \text{ cm} & h = 4.68 &
 \end{array}$$

Table 3.2: Optimal parameters found for the Fractional Filter Kernel (Section 2.4.2).

Fractional Filter Kernel shape

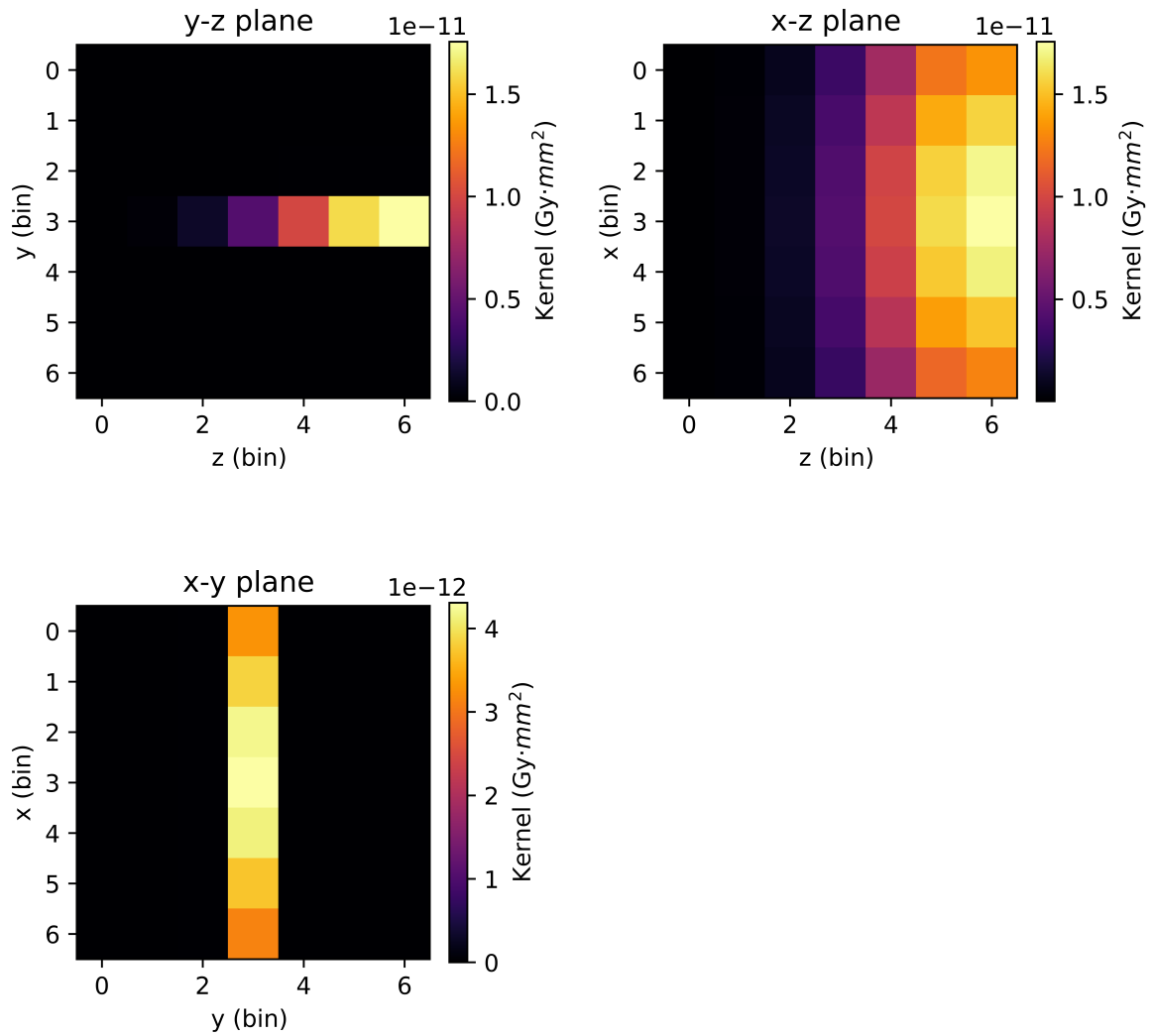


Figure 3.7: $7 \times 7 \times 7$ Fractional Filter kernel; in the y - z plane sliced at $x_{bin} = 4$, in the x - z plane sliced at $y_{bin} = 4$ and in the x - y plane sliced at $z_{bin} = 4$.

Comparison of the kernels

The optimisation of the Gaussian kernel is roughly 4x faster than optimising the FF kernel, this is probably because the Gaussian kernel has only 7 parameters, while the FF kernel has 11 parameters. The amplitudes of all three planes of the Gaussian Kernel in Figure 2.2 are in the order of 10^{-11} . The order of the amplitude for the FF kernel in Figure 3.7 is the same as for the Gaussian kernel, except for the x-y plane where the order is 10^{-12} . The shape of both kernels differs a lot from each other in all of the three planes.

y-z plane

The center of the Gaussian kernel is shifted and the spread in the y-direction is smaller than in the z-direction. The FF kernel is a line in the z-direction with increasing amplitude from left to right and has no spread in the y-direction.

x-z plane

The center of the Gaussian kernel is shifted and the spread in the z-direction is smaller than in the x-direction. The FF kernel is varying slightly in amplitude in the x-direction, while in the z-direction the kernel is varying more strongly.

x-y plane

The center of the Gaussian kernel is shifted and the spread in the y-direction is smaller than in the x-direction. The FF kernel is a line in the x-direction with increasing amplitude towards the top and bottom and has no spread in the y-direction.

3.3. Dose comparison

In this Section, the doses obtained through the Gaussian kernel (Gaussian dose) and Fractional Filter (FF dose) will be presented and compared to the secondary proton dose obtained from TOPAS as presented in Section 3.1.

3.3.1. Doses through convolution

The doses obtained through the FF kernel and the Gaussian Kernel are shown together with the target dose in Figure 3.8. On the left side in Figure 3.8 doses are presented in the y-z plane sliced at $x_{bin} = 25$ and on the right side the doses are presented in the x-y plane sliced at $z_{bin} = 4$. The (absolute) difference between the target dose and the other two doses is plotted in Figure 3.9. In Figure 3.10 the IDD in the z-direction is shown for the three doses with $\Delta x = \Delta y = 0.098cm$.

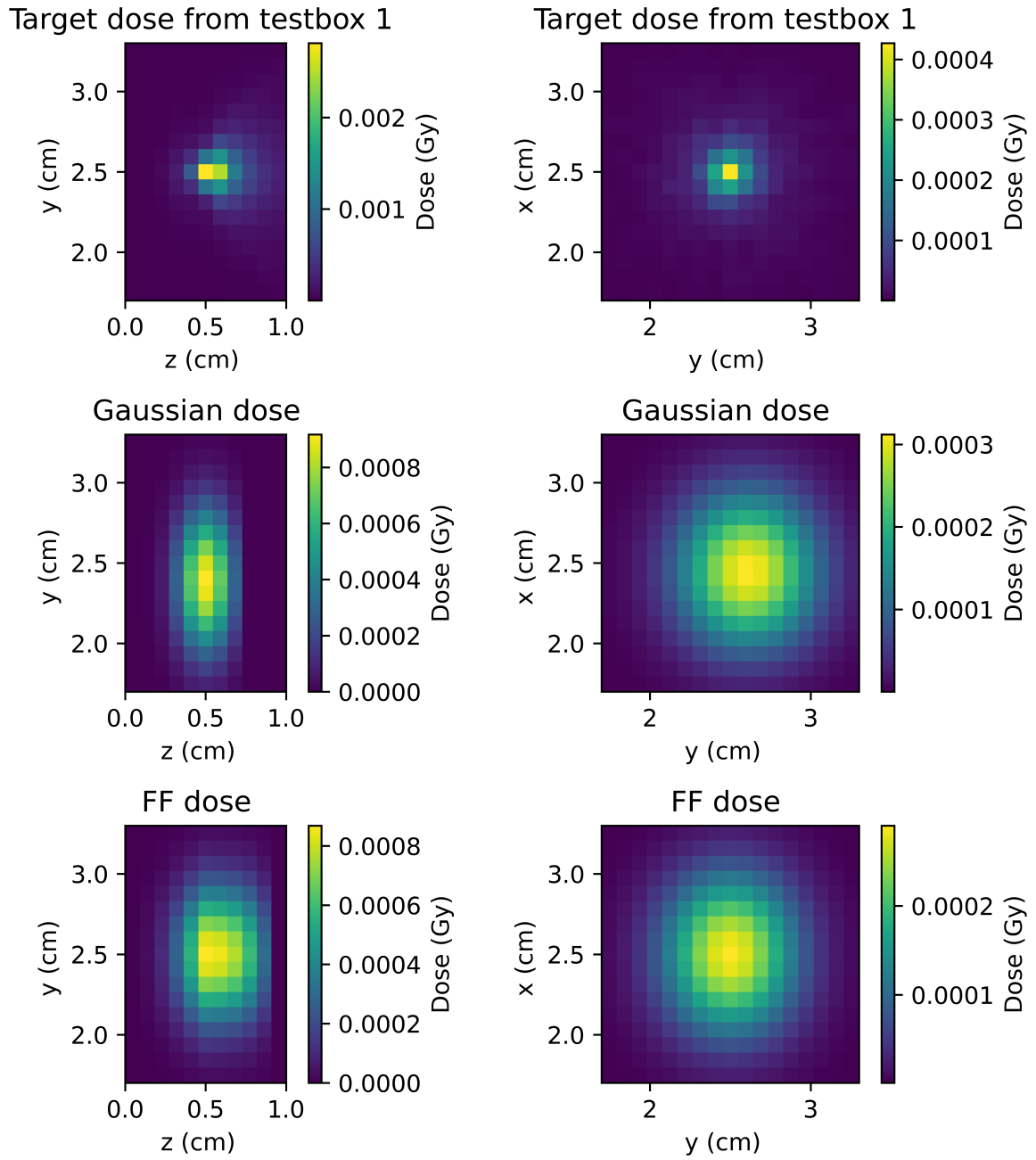


Figure 3.8: The secondary proton dose obtained through the Gaussian kernel and the Fractional Filter kernel together with the target dose. On the left side the dose distributions are presented in the y-z plane sliced at $x_{bin} = 2.5$ and on the right side the dose distributions are presented in the x-y plane sliced at $z_{bin} = 4$.

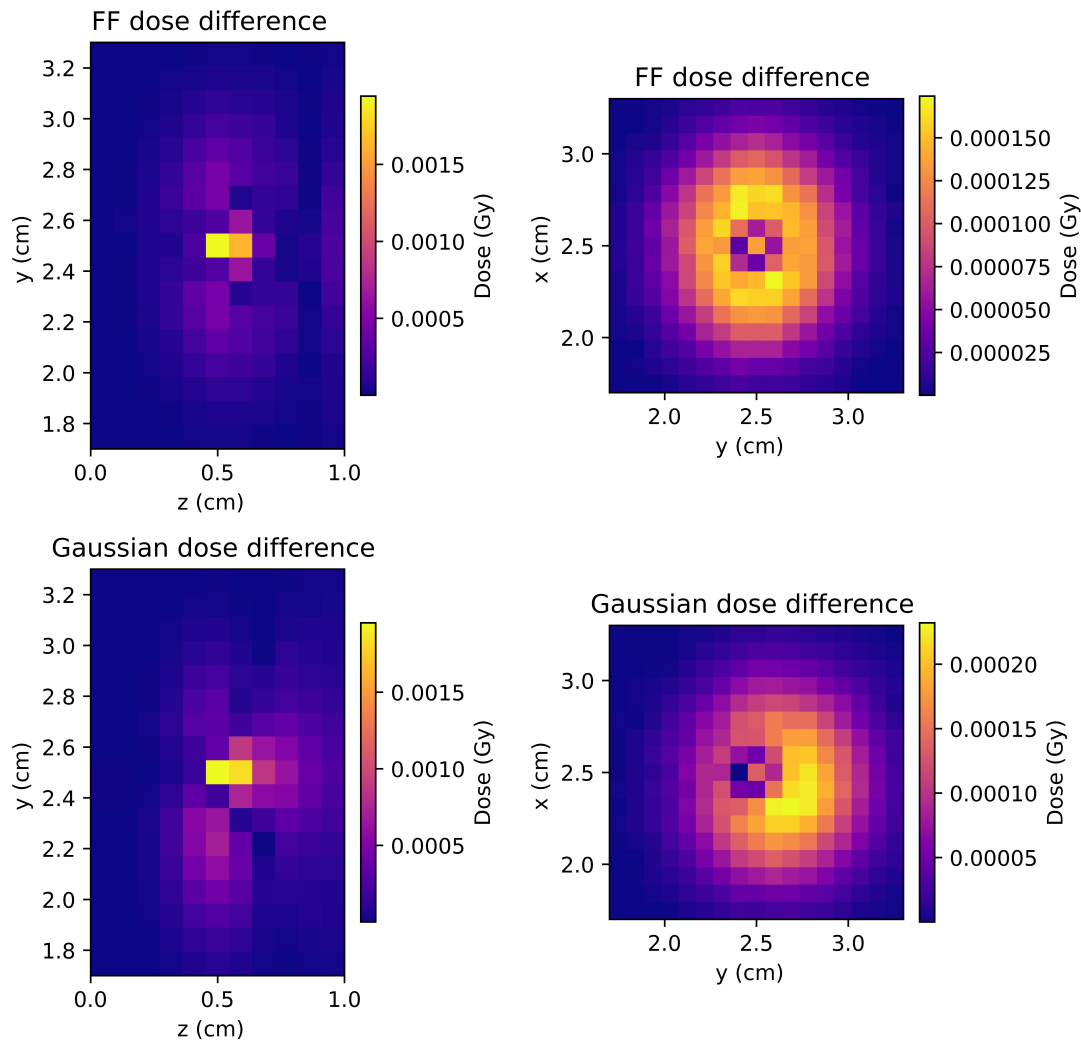


Figure 3.9: Plot of the difference between target dose and Gaussian dose and target dose and FF dose from Figure 3.8

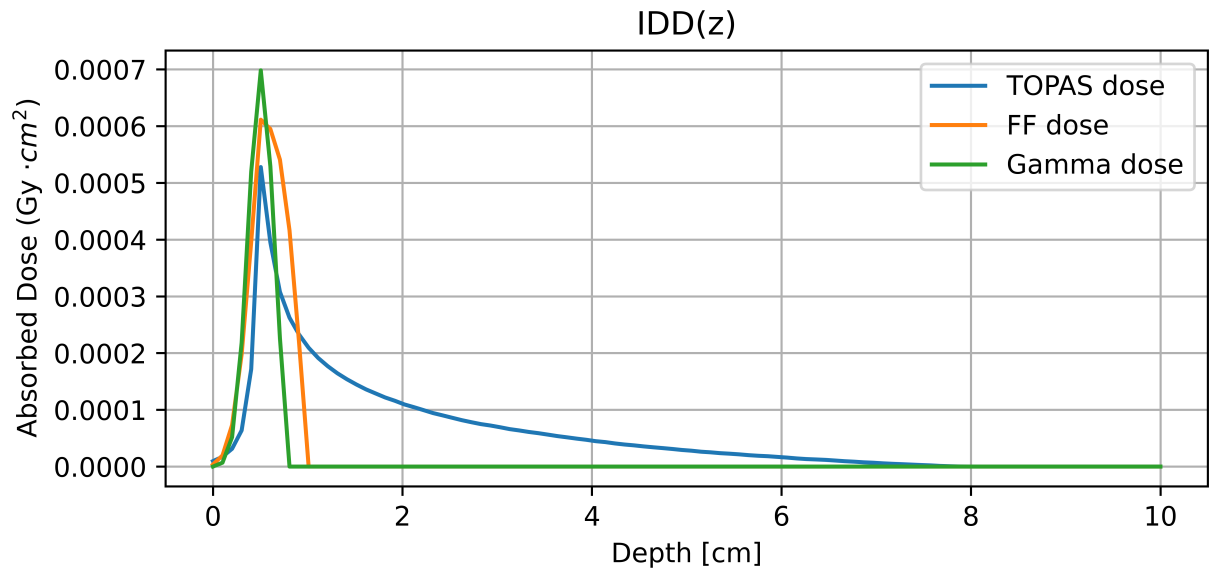


Figure 3.10: Plot of the integrated depth dose (IDD) for the TOPAS dose, Gaussian dose and FF dose in lateral direction.

In Figure 3.8, it can be seen that in the y - z plane the target dose is forward scattered and asymmetric. The Gaussian dose in the y - z plane is symmetric, while the FF dose is asymmetric. In the x - y plane the Gaussian dose and FF dose look similar, however they differ in amplitude.

In Figure 3.9, it can be seen that the biggest difference in amplitude in the y - z plane, is in the center of the plot. The FF kernel approximates the test dose better than the Gaussian dose, in the region around the center in y - z plane. The dose difference in the x - y plane for the FF kernel is symmetric, while the Gaussian dose difference is asymmetric. In the center region of both x - y plots in Figure 3.9, it can be seen that the dose difference is smaller, compared to when moving outside the center region. Furthermore, the amplitude in the x - y plane for the FF dose difference is overall smaller than the Gaussian dose difference.

From Figure 3.10 it can be seen that both doses approximate the TOPAS dose well before the Bragg peak, while after the Bragg peak, both convolutional doses approximate the TOPAS dose poorly. The IDD of the Gaussian and FF dose both fall off sharply to zero after a certain depth. Both peaks are higher than the peak from the test dose.

3.3.2. Gamma index comparison

The gamma index from Section 2.5.2 will be used to quantify the difference between the Gaussian dose and TOPAS dose and the FF dose and TOPAS dose. This gamma matrix is calculated with *calculate_gamma_index* algorithm in Python from the *phymedphys* library. For computational efficiency, the IDD representation of the doses will be used. From this gamma matrix a gamma histogram can be computed and a passing rate can be determined. The gamma histogram with passing rate for the Gaussian dose vs TOPAS dose and FF dose vs TOPAS dose can be seen in Figure 3.11 and Figure 3.12 respectively.

In Figure 3.11 and 3.12 it can be seen that the passing rate for the Gaussian dose and the FF dose is 17.65% and 29.41% respectively.

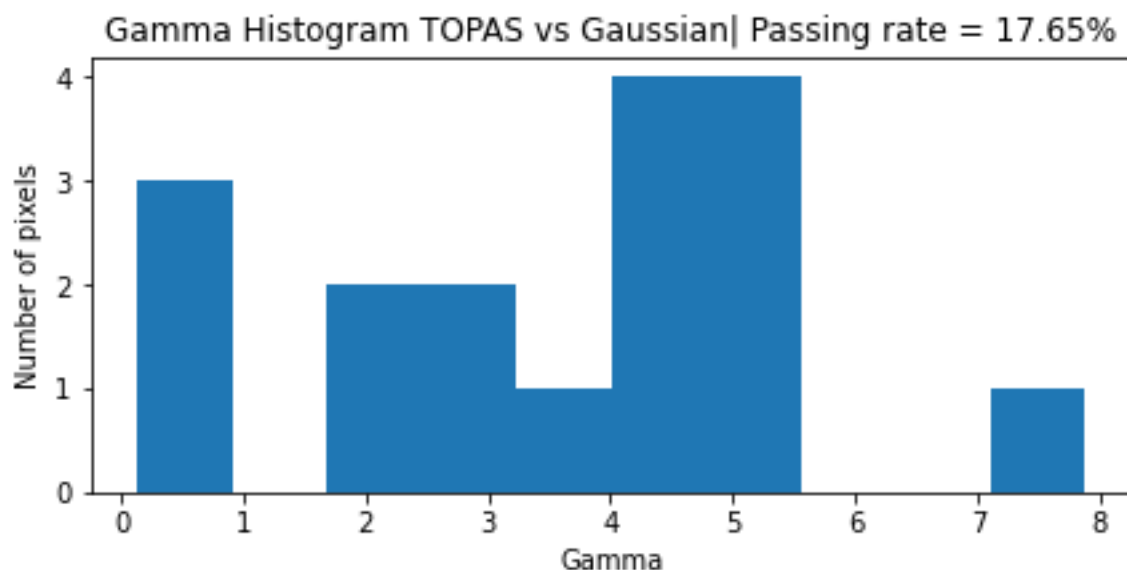


Figure 3.11: Gamma histogram plot for TOPAS dose vs. dose obtained via Gaussian kernel. The passing rate for the dose obtained from the Gaussian kernel is 17.65%.

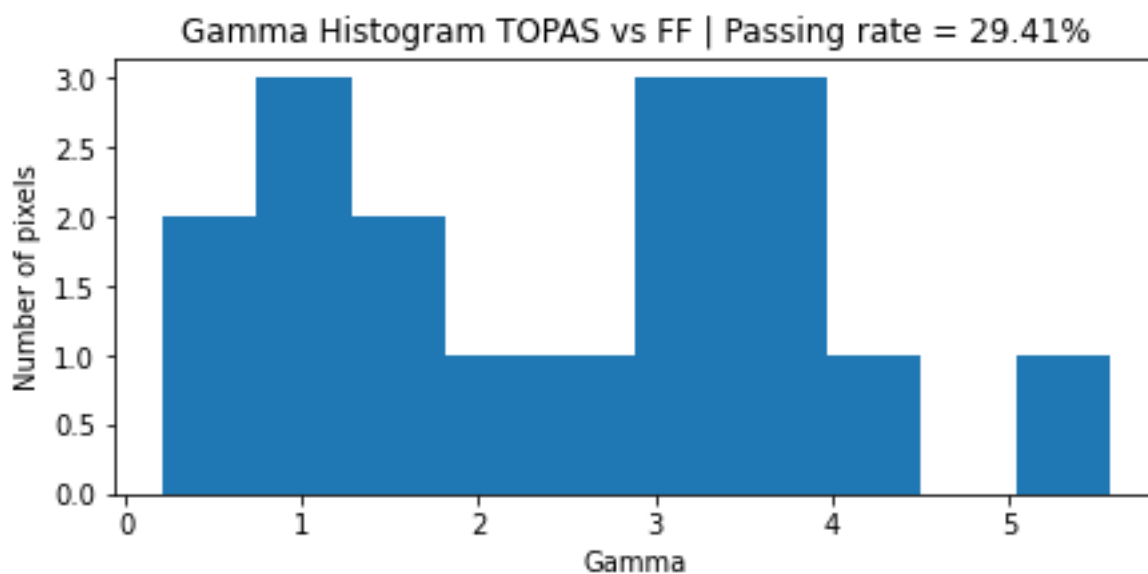
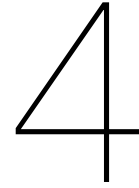


Figure 3.12: Gamma histogram plot for TOPAS dose vs. dose obtained via FF kernel. The passing rate for the dose obtained from the FF kernel is 29.41%.

3.3.3. Comparison of the convolutional dose distributions

It is expected that all of the target doses from the test boxes will have an asymmetric shape in the y-z plane, like the target doses in Figure 3.8. The FF kernel seems to be able to produce asymmetric doses, while the Gaussian kernel can only produce symmetric doses. Therefore, the FF kernel has an advantage over the Gaussian kernel, when looking at the shape in the y-z plane of the desired test dose. Furthermore, in the x-y plane the FF kernel produces a dose difference with an overall smaller amplitude than the Gaussian dose difference. Lastly, the passing rate of the FF dose is higher than the Gaussian dose. The only advantage that the Gaussian kernel has over the FF kernel is that it optimises 4x faster, but this is not an important factor.

This means that the FF kernel is a better kernel for approximating the TOPAS dose through a convolutional algorithm than the Gaussian kernel. However, it is expected that the secondary proton dose obtained through the FF kernel is not accurate enough to increase the accuracy of the deterministic semi-analytic algorithm. In fact, the secondary proton dose through the FF kernel might even decrease the accuracy of the semi-analytic algorithm, due to its inaccuracy. To check the influence of the convoluted secondary proton dose on the semi-analytic algorithm, it should be added to the total dose distribution and then be compared to a test dose.



Conclusion and recommendations

4.1. Conclusion

The Fractional Filter is better for estimating asymmetric dose distributions through convolutional methods than using a Gaussian kernel, due to the fact that a Fractional Filter kernel can produce both symmetric and asymmetric doses. It is not concluded in this research if the secondary dose obtained via convolutional methods is accurate enough to improve the accuracy of the dose distribution obtained through the deterministic semi-analytic algorithm. However, it is expected that the found Fractional Filter kernel will not suffice to increase the accuracy of the deterministic semi-analytic algorithm, due its low passing rate of 29.41%.

4.2. Recommendations for further research

For further research on this topic, there are several things that can be done. However, there is one step that is recommended to be done before moving towards the other improvement points. Namely, add the convolutional secondary proton dose to the total dose of the deterministic semi-analytic algorithm and see if its accuracy improves. Probably after this step, a more accurate convolutional secondary proton dose is desired. This can be done in several ways, firstly make use of the analytic derivative and/or Hessian matrix in the optimising process. This can have a positive impact on the accuracy of the produced secondary doses. However, this can prove quite difficult to implement for the Fractional Filter due to the complexity of the function. Secondly, a way of increasing accuracy is by training the parameters of the kernels using automatic differentiation [39] or artificial intelligence [40]. Thirdly, to approximate asymmetric doses the use of skew Gaussian functions (or derivatives of it for FF kernel) may prove useful for approximating asymmetric doses. [41]. Lastly, look into ways of producing asymmetric doses, such as the use of Half Gaussian Kernel (HGK) [42] or producing asymmetric kernels from symmetric kernels using piecewise linear perturbations [43].

Bibliography

- [1] WHO, *WHO report on cancer: setting priorities, investing wisely and providing care for all*. 2020, ISBN: 978-92-4-000130-5. [Online]. Available: <http://apps.who.int/bookorders..>
- [2] NCI, *What is cancer?* Accessed: 2022-06-06. [Online]. Available: <https://www.cancer.gov/about-cancer/understanding/what-is-cancer>.
- [3] “New approaches and procedures for cancer treatment: Current perspectives,” *SAGE Open Medicine*, vol. 9, p. 205 031 212 110 343, Jan. 2021, ISSN: 2050-3121. DOI: 10.1177/205031212111034366.
- [4] S. P. Jackson and J. Bartek, “The dna-damage response in human biology and disease,” *Nature*, vol. 461, pp. 1071–1078, 7267 Oct. 2009, ISSN: 0028-0836. DOI: 10.1038/nature08467.
- [5] R. Baskar, K. A. Lee, R. Yeo, and K.-W. Yeoh, “Cancer and radiation therapy: Current advances and future directions,” *International Journal of Medical Sciences*, vol. 9, pp. 193–199, 3 2012, ISSN: 1449-1907. DOI: 10.7150/ijms.3635.
- [6] A. R. Smith, “Vision : Proton therapy,” *Medical Physics*, vol. 36, no. 2, 2009. DOI: <https://doi.org/10.1118/1.3058485>. eprint: <https://aapm.onlinelibrary.wiley.com/doi/pdf/10.1118/1.3058485>. [Online]. Available: <https://aapm.onlinelibrary.wiley.com/doi/abs/10.1118/1.3058485>.
- [7] M. Schwarz, “Treatment planning in proton therapy,” *The European Physical Journal Plus*, vol. 126, pp. 1–10, Jul. 2011. DOI: 10.1140/epjp/i2011-11067-y.
- [8] Y. S. Yeom, K. Griffin, M. Mille, J. W. Jung, C. Lee, and C. Lee, “A dose voxel kernel method for rapid reconstruction of out-of-field neutron dose of patients in pencil beam scanning (PBS) proton therapy,” *Physics in Medicine & Biology*, vol. 65, no. 17, p. 175 015, Aug. 2020. DOI: 10.1088/1361-6560/abaa5f. [Online]. Available: <https://doi.org/10.1088/1361-6560/abaa5f>.
- [9] H. Paganetti, “Nuclear interactions in proton therapy: Dose and relative biological effect distributions originating from primary and secondary particles,” *Physics in Medicine and Biology*, vol. 47, pp. 747–764, 5 Mar. 2002, ISSN: 0031-9155. DOI: 10.1088/0031-9155/47/5/305.
- [10] W. D. Newhauser and R. Zhang, “The physics of proton therapy,” *Physics in Medicine and Biology*, vol. 60, R155–R209, 8 Apr. 2015, ISSN: 0031-9155. DOI: 10.1088/0031-9155/60/8/R155.
- [11] S. Park and J. Kang, “Basics of particle therapy i: Physics,” *Radiation oncology journal*, vol. 29, pp. 135–46, Sep. 2011. DOI: 10.3857/roj.2011.29.3.135.
- [12] J. J. Duderstadt and L. J. Hamilton, *Nuclear reactor analysis*. John Wiley Sons, 1976.
- [13] T. Burlacu, “Gauging the effect of energy straggling on proton dose distributions,” 2019. [Online]. Available: [http://repository.tudelft.nl/..](http://repository.tudelft.nl/)
- [14] M. Asadzadeh and T. Gebäck, “Analytical solutions for the pencil-beam equation with energy loss and straggling,” *PREPRINT*, vol. 41, Jan. 2011. DOI: 10.1080/00411450.2012.671207.
- [15] P. H., *Proton Therapy Physics*, H. Paganetti, Ed. CRC Press, Apr. 2016, ISBN: 9780367803551. DOI: 10.1201/9780367803551.
- [16] D. Wang, “A critical appraisal of the clinical utility of proton therapy in oncology,” *Medical Devices: Evidence and Research*, p. 439, Oct. 2015, ISSN: 1179-1470. DOI: 10.2147/MDER.S65594.
- [17] J. Perl, J. Shin, J. Schümann, B. Faddegon, and H. Paganetti, “Topas: An innovative proton monte carlo platform for research and clinical applications,” *Medical Physics*, vol. 39, pp. 6818–6837, 11 Oct. 2012, ISSN: 00942405. DOI: 10.1118/1.4758060.
- [18] J. Saini, E. Traneus, D. Maes, *et al.*, “Advanced proton beam dosimetry part i: Review and performance evaluation of dose calculation algorithms,” *Translational Lung Cancer Research*, vol. 7, pp. 171–179, 2 Apr. 2018, ISSN: 22186751. DOI: 10.21037/tlcr.2018.04.05.

- [19] V. Podlozhnyuk, "Image convolution with cuda," *NVIDIA Corporation white paper, June*, vol. 2097, no. 3, 2007.
- [20] S. B. Damelin and W. Miller Jr, *The Mathematics of Signal Processing*, ser. Cambridge Texts in Applied Mathematics. Cambridge University Press, 2011. DOI: 10.1017/CBO9781139003896.
- [21] IBM. "Convolutional neural networks." (1999), [Online]. Available: <https://www.ibm.com/cloud/learn/convolutional-neural-networks> (visited on 06/07/2022).
- [22] T. Archdeacon, *Correlation and Regression Analysis: A Historian's Guide*. University of Wisconsin Press, 1994, ISBN: 9780299136505. [Online]. Available: <https://books.google.nl/books?id=tptmAAAAAAAJ>.
- [23] B. Kalaf, "Application of the downhill simplex algorithm for solving aggregate production planning problems," *Sci.Int.(Lahore)*, vol. 29, pp. 1075–1081, Oct. 2017.
- [24] J. R. Shewchuk *et al.*, *An introduction to the conjugate gradient method without the agonizing pain*, 1994.
- [25] G. Charpiat, M. Hofmann, and B. Schölkopf, "Kernel methods in medical imaging," in *Handbook of Biomedical Imaging*, Springer, 2015, pp. 63–81.
- [26] M. de Moraes Marim, B. Zhang, J.-C. Olivo-Marin, and C. Zimmer, "Improving single particle localization with an empirically calibrated gaussian kernel," in *2008 5th IEEE International Symposium on Biomedical Imaging: From Nano to Macro*, 2008, pp. 1003–1006. DOI: 10.1109/ISBI.2008.4541168.
- [27] H. S. Lee and J. W. Jeon, "Accelerating image processing on fpgas using hls and pynq," in *2020 IEEE International Conference on Consumer Electronics - Asia (ICCE-Asia)*, 2020, pp. 1–2. DOI: 10.1109/ICCE-Asia49877.2020.9277085.
- [28] A. Asjad and M. Deriche, "A new approach for salt dome detection using a 3d multidirectional edge detector," *Applied Geophysics*, vol. 12, pp. 334–342, Sep. 2015. DOI: 10.1007/s11770-015-0512-2.
- [29] R. C. Gonzalez and R. E. Woods, *Digital Image Processing*, 4th ed. Upper Saddle River, NJ: Pearson, Mar. 2017.
- [30] N. Kanopoulos, N. Vasanthavada, and R. Baker, "Design of an image edge detection filter using the sobel operator," *IEEE Journal of Solid-State Circuits*, vol. 23, no. 2, pp. 358–367, 1988. DOI: 10.1109/4.996.
- [31] K. Kang, M. Shelley, and H. Sompolinsky, "Mexican hats and pinwheels in visual cortex," *Proceedings of the National Academy of Sciences*, vol. 100, no. 5, pp. 2848–2853, 2003.
- [32] S. Das, *Functional fractional calculus*, en, 2nd ed. Berlin, Germany: Springer, Jun. 2011.
- [33] J. Zamora, J. A. Cruz Vargas, A. Rhodes, L. Nachman, and N. Sundararajan, "Convolutional filter approximation using fractional calculus," in *2021 IEEE/CVF International Conference on Computer Vision Workshops (ICCVW)*, 2021, pp. 383–392. DOI: 10.1109/ICCVW54120.2021.00047.
- [34] X. R. Zhu, F. Poenisch, M. Lii, *et al.*, "Commissioning dose computation models for spot scanning proton beams in water for a commercially available treatment planning system," *Medical Physics*, vol. 40, p. 041 723, 4 Apr. 2013, ISSN: 00942405. DOI: 10.1118/1.4798229.
- [35] M. Hussein, C. Clark, and A. Nisbet, "Challenges in calculation of the gamma index in radiotherapy – towards good practice," *Physica Medica*, vol. 36, pp. 1–11, Apr. 2017. DOI: 10.1016/j.ejmp.2017.03.001.
- [36] C. E. T. Haar, "Robustness recipes for proton therapy polynomial chaos expansion as a tool to construct robustness recipes for proton therapy," 2018.
- [37] S. Bresciani, A. D. Dia, A. Maggio, *et al.*, "Tomotherapy treatment plan quality assurance: The impact of applied criteria on passing rate in gamma index method," *Medical Physics*, vol. 40, p. 121 711, 12 Nov. 2013, ISSN: 00942405. DOI: 10.1118/1.4829515.
- [38] H. Elsayed, "Quantifying secondary particle dose contributions in proton therapy," 2022. DOI: <http://resolver.tudelft.nl/uuid:c52c63aa-9af8-420b-8d88-fca9ace7b946>.

- [39] A. G. Baydin, B. A. Pearlmutter, A. A. Radul, and J. M. Siskind, "Automatic differentiation in machine learning: A survey," *Journal of Machine Learning Research*, vol. 18, no. 153, pp. 1–43, 2018. [Online]. Available: <http://jmlr.org/papers/v18/17-468.html>.
- [40] M. Claesens and B. De Moor, "Hyperparameter Search in Machine Learning," *arXiv e-prints*, Feb. 2015.
- [41] S. Nadarajah and S. Kotz, "Skewed distributions generated by the normal kernel," *Statistics & Probability Letters*, vol. 65, pp. 269–277, Nov. 2003. DOI: 10.1016/j.spl.2003.07.013.
- [42] H. Abdulrahman, M. Baptiste, and P. Montesinos, "Oriented asymmetric kernels for corner detection," Aug. 2017, pp. 778–782. DOI: 10.23919/EUSIPCO.2017.8081313.
- [43] J. Star-Lack, M. Sun, A. Kaestner, *et al.*, "Efficient scatter correction using asymmetric kernels," in *Medical Imaging 2009: Physics of Medical Imaging*, E. Samei and J. Hsieh, Eds., International Society for Optics and Photonics, vol. 7258, SPIE, 2009, pp. 644–655. DOI: 10.1117/12.811578. [Online]. Available: <https://doi.org/10.1117/12.811578>.